Appl. Phys. B 74, 175–183 (2002)
DOI: 10.1007/s003400100777

Applied Physics B
Lasers and Optics

L.A. RIBAROV[1]
J.A. WEHRMEYER[1]
R.W. PITZ[1,✉]
R.A. YETTER[2]

Hydroxyl tagging velocimetry (HTV) in experimental air flows

[1] Department of Mechanical Engineering, Vanderbilt University, Nashville, TN 37 235, USA
[2] Department of Mechanical and Nuclear Engineering, Pennsylvania State University, University Park, PA 16 802, USA

Received: 3 July 2001/Revised version: 6 November 2001
Published online: 17 January 2002 •

ABSTRACT The new nonintrusive instantaneous molecular flow tagging method, hydroxyl tagging velocimetry (HTV), previously demonstrated only for high-temperature reacting flows, is now demonstrated in low-temperature (300 K) ambient air flowfields. Single-photon photodissociation of ground-state H_2O by a $\sim$ 193-nm ArF excimer laser 'writes' very long grid lines ($>$ 50 mm) of superequilibrium OH and H photoproducts in a room air flowfield due to the presence of ambient H_2O vapor. After displacement, the positions of the OH tag lines are revealed through fluorescence caused by $A^2\Sigma^+ (v' = 0) \leftarrow X^2\Pi_i (v'' = 0)$ OH excitation using a pulsed frequency-doubled dye laser with an operating output wavelength of $\sim$ 308 nm. The dye 'read' laser accesses the strong $Q_1(1)$ line, compensating for the relatively weak 193-nm absorption of room-temperature H_2O. The weak absorption of ground vibrational state H_2O has previously precluded the use of HTV at low temperatures, since previous HTV systems relied on a KrF excimer 'read' laser that could only access a weak $(3 \leftarrow 0)$ OH transition. The instantaneous velocity field is determined by time-of-flight analysis. HTV tag lifetime comparisons between experimental results and theoretical predictions are discussed. Multiple-line tag grids are shown displaced due to an experimental air flowfield, thus providing 2-D multipoint velocity information. Due to the instantaneous nature of the HTV tag formation, HTV is particularly suitable for, but not limited to, a variety of fast flowfield applications including nonreacting base flows for high-speed projectiles and low-temperature hypersonic external or internal flows.

PACS 42.62.Fi; 47.80.+v; 82.50.Fv

1 Introduction

Nonintrusive velocity measurements in experimental gas flowfields are performed routinely with molecular velocimetry methods. Molecular velocity methods involving the Doppler shift of scattered light have been previously demonstrated [1]. Doppler shifts of sodium [2], iodine [3], copper [4], and nitric oxide [5] have been used for gas-flow velocimetry in laser-induced fluorescence (LIF) experiments. The Doppler shift of Rayleigh-scattered laser light has been measured with Fabry–Perot interferometers and molecular filters to yield a velocity field [6, 7]. Often, in such high-speed flows, Doppler-shift methods are relatively inaccurate at low velocities due to the extremely small Doppler shift.

Molecular tagging, another type of molecular velocimetry method, does not necessarily involve a Doppler shift and hence can be amenable to both low- and high-speed experimental gas flowfields. The molecular marker is written onto the interrogated gas and velocity is determined by computing the displaced marker's position over a known time period. Several molecular tagging methods rely on seeding of the gas flow prior to its interrogation by the laser light sources. Laser-induced phosphorescence of biacetyl, $(CH_3CO)_2$, lines has been used for visualization of N_2 flows [8, 9]. Grids of NO have recently been demonstrated in gas flows by seeding the flow with NO_2 [10]. Gas-phase velocity-field measurements in dense sprays have been recently shown by seeding with tert-butyl nitrate, $(CH_3)_3CONO$, to produce NO grid lines [11]. Such molecular methods with chemical additives are often undesirable from an environmental and/or safety aspect, and in large-scale applications they can be prohibitively costly.

Several time-of-flight unseeded molecular flow tagging velocimetry methods have been successfully developed, such as two-photon water vapor dissociation [12], Raman excitation plus laser-induced electronic fluorescence (RELIEF) of O_2 [13], and ozone tagging velocimetry (OTV) [14]. Nonlinear methods [12, 13] generally produce shorter lines due to the signal's inverse dependence on the beam diameter squared. Also, elevated temperatures can be detrimental to some unseeded tagging methods [13, 14].

A relatively new nonintrusive velocimetry technique, hydroxyl tagging velocimetry (HTV), has recently been developed for high-temperature reacting flows [15]. In this technique, grid lines of OH are written in a moving gas stream by photodissociating the vibrationally excited H_2O present in these high-temperature combustion flows. A detailed description of the vibrationally excited H_2O photochemistry and the high-temperature application of the HTV method is published elsewhere [15, 16]. For its previous high-temperature application, HTV used two excimer lasers. A pulsed tunable 193-nm ArF excimer laser is the 'write' laser and a pulsed tunable narrow-band 248-nm KrF excimer laser is used as the 'read'

✉ Fax: +1-615/343-6687, E-mail: robert.w.pitz@vanderbilt.edu

laser. The KrF laser accesses only the $A^2\Sigma^+\,(v'=3) \leftarrow X^2\Pi_i\,(v''=0)$ OH band, whose resulting fluorescence is relatively weak due to predissociation, compared to that produced from $(0 \leftarrow 0)$ or $(1 \leftarrow 0)$ pumping. An extensive review of OH LIF research (among other laser diagnostic methods) is found in [17]. Because of the weakness of fluorescence from the OH lines pumped by the KrF excimer laser, only high-temperature flows have been successfully probed. These flows contain significant populations of vibrationally excited H_2O, and these vibrational levels have 193-nm photodissociation cross sections several orders of magnitude higher than the ground vibrational state of H_2O [15, 16]. Thus the weakness of the 'read' process has been offset by the strength of the 'write' process.

In order to use the HTV technique at low temperatures, where only ground vibrational state H_2O exists, with its low 193-nm absorption cross section, a strong OH fluorescence 'read' process must be used. In this work, a frequency-doubled dye laser pumped by a Nd–YAG laser (also frequency-doubled) replaces the KrF excimer as a 'read' source to demonstrate the HTV's applicability to low-temperature flowfields. By operating the frequency-doubled dye laser at ~ 308 nm, the vibrational transitions of the $A^2\Sigma^+\,(v'=0) \leftarrow X^2\Pi_i\,(v''=0)$ OH band are accessed. These $(0 \leftarrow 0)$ transitions result in fluorescence that is about two orders of magnitude (where the ratio of the Einstein 'B' coefficients for the $(3 \leftarrow 0)$ and $(0 \leftarrow 0)$ transitions respectively is $B_{30}/B_{00} \cong 0.006$ [18]) stronger than that for the $(3 \leftarrow 0)$ transitions previously used for the high-temperature HTV work [15, 16]. These strongly fluorescing OH $(0 \leftarrow 0)$ transitions compensate for the relatively weak 193-nm photodissociation cross section of ground vibrational state H_2O [15], allowing HTV to be applied to low-temperature (300 K) flowfields.

2 Experimental system

A schematic of the experimental system is shown in Fig. 1. The low-temperature HTV demonstration consists of two laser light sources. A tunable Lambda Physik COMPex-150T 193-nm ArF excimer laser is the write laser. The output of the narrow-band ArF excimer laser (~ 150 mJ/pulse, 0.003-nm line width, 0.2-mrad divergence at FWHM) is divided into a set of three beams and a set of four beams, with both sets crossing in the flowfield. The ArF beams are focused to 0.5-mm beam waist by a 0.5-m focal length (f.l.) spherical lens. The tunable ArF excimer laser is operated in its broadband mode ($\sim$ 1-nm line width) since the H_2O absorption band is a broad continuum lacking any distinct absorption lines [15]. The total distance traveled by each of the ArF grid lines is over 1 m in (unpurged) room air and leads to about a 16% loss in energy from laser exit to the measurement zone.

The output of a Continuum Powerlite Nd–YAG laser (532 nm) is frequency-doubled and used to pump a Continuum ND6000 dye laser whose output is frequency doubled to ~ 308 nm to provide the (10 mJ/pulse, tunable, 0.05-cm^{-1} bandwidth) read laser. A solution of xanthene rhodamine R640 perchlorate red dye (Exciton, Inc.) crystals diluted in high-purity methanol is used in the oscillator and amplifier

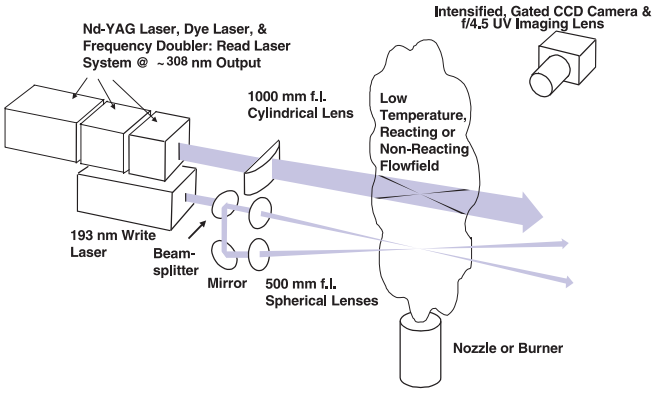

FIGURE 1 Schematic of low temerature HTV experimental system showing optics needed for two OH tag lines only

circuits of the Continuum ND6000 dye laser. The 308-nm light output of the dye laser is focused by a 1-m f.l. cylindrical lens to a sheet of 20-mm by 0.5-mm cross section. Images from the measurement volume were collected through a multi-element UV imaging lens (Nikon, UV-Nikkor F/4.5, $f = 105$ mm) coupled to a gated Princeton Instruments ICCD camera (576×384 array, 22-μm pixels). The gating time was typically 50 ns. A 3-mm-thick butyl acetate filter (passing wavelengths longer than 255 nm) was placed in front of the UV lens to reject the strong O_2 fluorescence lines caused by the 193-nm ArF excimer laser, thus preventing the appearance of O_2 fluorescence on the CCD image from photocathode image persistence [14]. The collected images were digitized and stored on a personal computer. The output of the read dye laser is tuned to excite the strong $A^2\Sigma^+\,(v'=0) \leftarrow X^2\Pi_i\,(v''=0)$ OH transition.

2.1 OH *tag spectral identification, formation, and lifetime*

Figure 2b shows the fluorescence excitation spectrum for the flow tag measured in quiescent room air conditions (297 K, 40% RH) for a $\sim$ 1-nm range of the tunable dye laser. The dye laser does have a wider tuning range; however, to keep the dye laser output relatively strong (and close to its peak value), its range was kept at around 1 nm, between ~ 307.3 nm ($32\,545\ cm^{-1}$) and ~ 308.2 nm ($32\,445\ cm^{-1}$). The dye laser's output for this range was in the relatively linear section of the laser dye-tuning curve; hence, the laser's output power was normalized in a linear fashion. The spectral signature of OH-LIF is clearly identified in this excitation and transitions are assigned by comparing the experimental results to earlier spectral data [19, 20] as well as to a simulated spectrum (Fig. 2a) for the same initial conditions [21]. As seen from the spectra, at $32\,474.433\ cm^{-1}$ (307.935 nm) the $Q_1(1)$ is the strongest line to pump in the portion of the $A^2\Sigma^+\,(v'=0) \leftarrow X^2\Pi_i\,(v''=0)$ OH band that is accessible by the dye laser.

The dissociated H_2O fraction can be calculated in the limit of weak absorption ($\sigma_i n_i L < 1$) and is given by [16]

$$(n_{\mathrm{di}})/(n_i) = (\sigma_i E)/(h\nu A) \qquad (1)$$

where, in the i^{th} vibrational level, n_i is the number density of water, n_{di} is the number density of dissociated water,

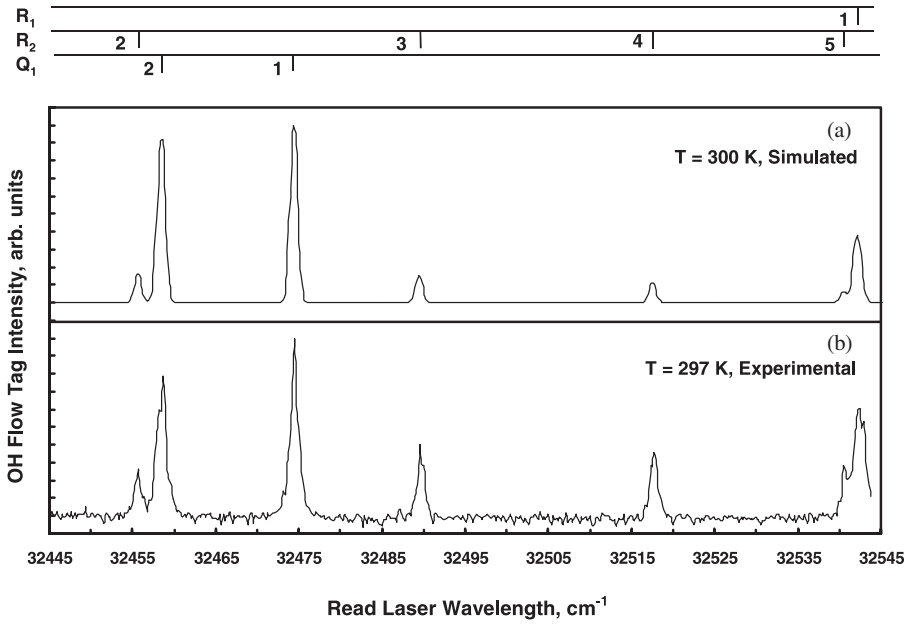

FIGURE 2 Room temperature (300 K) HTV LIF excitation spectra showing the strong $Q_1(1)$ transition of the $A^2\Sigma^+ (v' = 0) \leftarrow X^2\Pi_i (v'' = 0)$ OH band. Curves are normalized to the $Q_1(1)$ line showing (a) simulation by LIFBASE, and, (b) experimental spectrum

σ_i is the absorption cross section, E is the laser pulse energy, h is Planck's constant, v is the frequency of light, L is the length of the H_2O region through which the laser beam travels, and A is the area of the laser beam. At room temperature (300 K), all the H_2O molecules are in the ground vibrational state with three fundamental frequencies (v_1, v_2, v_3) for three modes: symmetric stretch ($v_1 = 3651.7\,\text{cm}^{-1}$), symmetric bend ($v_2 = 1595.0\,\text{cm}^{-1}$), and asymmetric stretch ($v_3 = 3755.8\,\text{cm}^{-1}$). For 193 nm, the ground-state (0, 0, 0) absorption cross section is small, $8 \times 10^{-22}\,\text{cm}^2$ [22], and leads to about 1% dissociation of H_2O vapor in room air for typical experimental conditions (10 mJ/pulse, 20 ns, 0.5-mm-diameter laser beam, ~ 0.25-GW/cm^2 irradiance). This relatively low pulse energy (as compared to typical nonlinear methods with ~ 50-GW/cm^2 irradiance [13]) can be very beneficial particularly in measurements that might be conducted near windows or in gases containing particles that might otherwise tend to break down (i.e. ionize) under the high laser irradiance levels that are required for excitation by nonlinear methods. For typical room air conditions of 24.4 °C (297.4 K) and 40% RH, 1% dissociation of H_2O leads to a number density of $\sim 3 \times 10^{15}$OH molecules/cm^{-3} (125 ppm). The OH tag is formed immediately by 193-nm photodissociation from the ArF excimer laser pulse. The flow tag's formation is limited only by the excimer pulse width, which is ~ 20 ns. This short formation time makes HTV amenable, but not limited, to high-speed flows, where the time delay between write and read lasers may be < 1 μs.

The strength of the OH tag 'read' signal depends on the initial mole fraction of H_2O vapor present in the ambient air (related to RH and temperature), the delay time between the write and read laser pulses, and the molecular diffusion that takes place at room temperature for the OH molecule. A series of single-shot images of the experimental flowfield (air jet) were taken to address the effect of delay time on the OH tag signal strength. The signal of a typical laser line segment in the HTV grid was integrated and averaged at various times to determine the decay of the integrated signal. This value is independent of the diffusion rate. A value for background (fairly constant from shot-to-shot) was subtracted from a corresponding total signal value to yield experimental points on the curve as shown in Fig. 3.

To predict the lifetime of the low-temperature OH tag, the CHEMKIN II thermodynamic database and the SENKIN chemical kinetics solver [23] are used with an air-chemistry mechanism consisting of a set of 109 reversible reactions (27 species) as shown in the appendix. A constant-pressure adiabatic system was simulated that initially contains an equilibrium humid air mixture to which is added a certain amount of OH and H photoproducts. As calculated above, ~ 1% of ambient H_2O vapor (40% relative humidity, 297 K) is photodissociated into ~ 125 ppm of OH and H atoms by the ArF write laser. Figure 3 shows a comparison between the SENKIN predictions for OH concentration (with either 0 or 200 ppm of initial O-atom concentration) and experimentally determined OH tag signal intensity that is both normalized and plotted as a function of delay time between the write and read lasers. The rates of two significant OH recombination pathways ($R4$, $R14$) were modified from their previous values [14], thus better approximating the experimental conditions. With no O atoms, OH is rapidly depleted primarily via the chain sequence ($R9$, $R13$) where a fast formation of HO_2 ($R9$) leads to OH depletion ($R13$). However, a small amount of O atoms (200 ppm) will be present based on the expected $\sim 0.05\%$ O_2 dissociation by the broadband ArF laser. With the O atoms present, there is a much better comparison between the simulation and experiment. The initial O-atom concentrations were varied over a wide range (100–4100 ppm) of input conditions to the SENKIN solver without any appreciable changes in the OH-depletion rates. The initial presence of O atoms depletes HO_2 and additionally regenerates OH through ($R10$). Slight under-prediction of the experimental results by the mechanism could be attributed to uncertainties in both the initial conditions as well as rate-constant parameters, notably for $R13$, which has the greatest uncertainty.

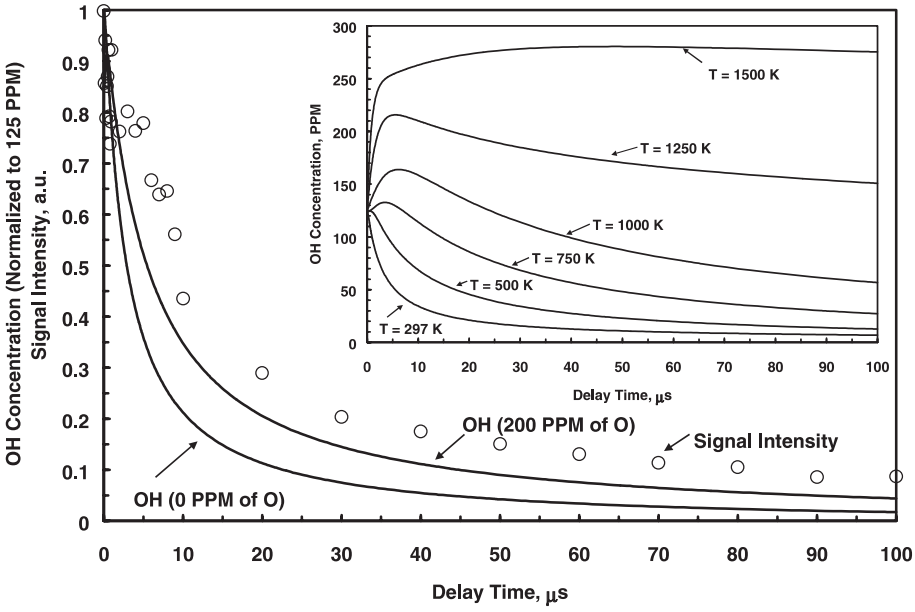

FIGURE 3 Average HTV signal intensity (experimental value independent of the diffusion rate) and OH concentration (SENKIN predictions, with- and without initial O atoms) curves as function of delay time (μs) between write and read laser. Experimental conditions: room air temperature (297 K, 40% RH) airflow. Inset features OH time histories (for 125 ppm initial OH mole fraction and 200 ppm initial O mole fraction) as funktion of various initial temperatures (K) and constant pressure (1 atm)

To determine the effect of temperature on the OH tag lifetime, the OH time histories were simulated for several different initial temperatures (see Fig. 3, inset), ranging from 297 K to 1500 K, where constant initial mole fractions of OH are assumed (125 ppm) and with 200 ppm of O. While low temperatures (< 500 K) have a minimal effect on the initial rise in OH concentration, it is observed that at higher temperatures (> 600 K) additional amounts of OH are produced at very short delay times (< 10 μs). These results agree with previously demonstrated SENKIN simulations of high-temperature combustion environments [15]. All temperature cases tend to fall back to the equilibrium OH concentrations (not shown) as the delay time increases significantly, especially for the initial higher-temperature cases. The inset in Fig. 3 shows results only for the first 100 μs of OH time histories since typical HTV write/read delay times are in that range (0–100 μs).

2.2 *HTV imaging in an air jet*

Tagging measurements were made in an air jet created by the inner core (12.5-mm diameter) of a small Hencken burner nozzle (25-mm diameter, including co-flow) emanating into a quiescent surrounding environment. The measured flow rates (at 300 K, 1 atm) were ∼ 205 slpm, yielding a theoretical average jet exit velocity value of $u \sim 28$ m/s and a local Reynolds number of $\mathrm{Re}_d = 23\,000$ ($d = 12.5$ mm). Variable time delays between the write and read lasers were used to study the OH tag's lifetime. A 3×4 grid of tag lines was created by splitting the 193-nm write laser beam into seven beams, each focused by a separate 500-mm f.l. lens. The resulting twelve crossing points provide unambiguous locations to determine displacement. Figure 4b shows a typical instantaneous image of the displaced HTV grid for a 30-μs delay. This is for a location immediately downstream from the nozzle's exit (1–2 diameters) near the air jet's centerline. The flow proceeds from the figure's lower right corner to the upper left corner. Slight variations in tag lines' intensity are attributed to unequal splitting of the laser beam, nonuniform intensity profiles of the dye and excimer lasers, system alignment, and possible beam-transmission problems. The 'dots' in the images are produced by light scattering from dust particles in the air. Figure 4a shows another image of the same HTV grid for a write–read delay of 0 μs, thus providing initial locations for the grid lines' crossing points in the flow. Based on the initial and final locations of these crossing points, and knowing the time delays, one can establish velocity-vector profiles. The initial locations of the grid lines are indicated in Fig. 4b by the superimposed initial grid (in black) and displacement vectors (in black). The crossing points were numbered arbitrarily for convenient location and identification of a specific displacement vector. For example, the average length estimate for displacement vector No. 6 is 1.06 mm, which, when divided by the 30-μs write–read delay time, yields a measured velocity of 35.3 m/s. This experimental value is close to the theoretically expected value for the average jet exit velocity of ∼ 28 m/s. Since the fluorescence emission is mostly from $v' = 0$ due to the $(0 \leftarrow 0)$ pumping of OH at ∼ 308 nm, the fluorescence light is very close to the laser wavelength and hence it is difficult to separate. This results in elastic particle scattering that can be minimized (or even avoided) by using, say, $A^2\Sigma^+\,(v' = 1) \leftarrow X^2\Pi_i\,(v'' = 0)$ OH excitation at ∼ 285 nm to read the HTV grid, and imaging only $(1 \rightarrow 1)$ emission at 308 nm.

Considering the local experimental conditions one can compute the appropriate Kolmogorov microscales for time, length, and velocity [24] in the air jet. For 300 K and 1 atm, the kinematic viscosity of air is $v \sim 1.52 \times 10^{-5}\,\mathrm{m^2/s}$ [25]. The turbulent kinetic energy dissipation rate per unit mass is $\varepsilon = (u_{\mathrm{rms}}^3/L_0)$ and its value is $\sim 40 \times 10^3\,\mathrm{m^2/s^3}$, where u_{rms} is the average turbulent fluctuating velocity and L_0 is the integral length scale. The value of u_{rms} can be assumed to be 20% of the expected local jet velocity, $u \sim 28$ m/s. The integral length scale, L_0, is given as $L_0 \sim 0.7\,R_{\mathrm{u}}$, where R_{u} is the radius at which the turbulent velocity is halfway between the centerline and the free-stream values [26]; in this

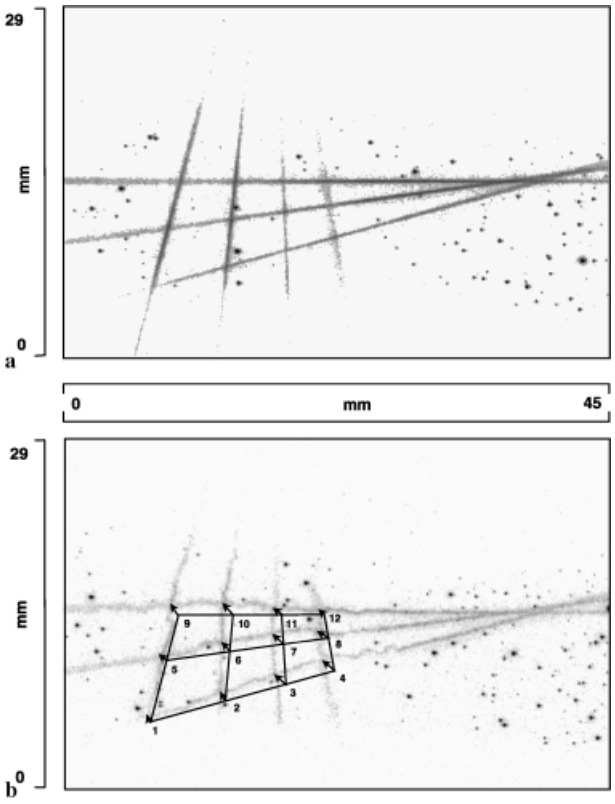

FIGURE 4 HTV images in room temperature (297 K, 40% RH) airflow (flow moving from lower right to upper left corners in both images). Write laser: ArF excimer at 193 nm. Read laser: frequency doubled dye at 308 nm. Delays: **a** 0 μs; **b** 30 μs

work $L_0 \sim 4.4$ mm. Thus, one can compute the corresponding value for the Kolmogorov length scale, $\eta = (\upsilon^3/\varepsilon)^{0.25}$, to be approximately equal to 17 μm. Similarly, the values for the Kolmogorov time scale, $t = (\upsilon/\varepsilon)^{0.5}$, and the Kolmogorov velocity scale, $s = (\upsilon\varepsilon)^{0.25}$, were found to be approximately 20 μs and 0.9 m/s respectively. With the current HTV setup, we cannot measure the velocity eddies at the Kolmogorov length scale (the smallest turbulence length scale), but we could resolve fluctuations at the integral length scale (the largest turbulence length scale).

The velocity-measurement uncertainty is dominated by the displacement-measurement uncertainty, since the write–read delay is known within 5 ns or ∼ 0.02% of the 30-μs value used for the delay time. The displacement-measurement uncertainty depends on uncertainties in measuring the initial and final grid locations as well as the width of the tag lines. The final location and tag-line width uncertainties are higher due to the molecular diffusion effects, which tend to spread out the tag line from its initial tightly focused diameter. As can be seen in Fig. 4b, the lines of OH diffuse in the room air temperature flow. The OH line diffusion broadening can be estimated from [27]:

$$w = \left[8\ln(2)\tau D + w_0^2\right]^{1/2} \tag{2}$$

where w is the tag-line width after a delay time τ, w_0 is the initial tag-line width, and $D_{\mathrm{OH}} = 0.27\ \mathrm{cm}^2/\mathrm{s}$ is the appropriate binary diffusion coefficient for OH into N_2 at 300 K [28]. This gives an expected tag-line width of ∼ 0.504 mm for $\tau = 30$ μs. This is based on a directly measured value for $w_0 \sim 0.5$ mm, which is typical for the experimental HTV images at 0-μs delay time. The average value for w in Fig. 4b is slightly higher than 0.504 mm, being closer to ∼ 0.6 mm. This could be at least partially explained by the idea of additional formation of OH from H photoproduct as evidenced from (*R*9, *R*10) with 200 ppm of O atoms. Before H reacts to form OH, it diffuses from the tag at a faster rate than does the heavier OH molecule. The binary diffusion coefficient for H into N_2 at 300 K is $D_{\mathrm{H}} \sim 1.09\ \mathrm{cm}^2/\mathrm{s}$ and as a result the tag-line width is predicted to be ∼ 0.518 mm. Some localized but minimal heating (2–6 K) due to the laser beams may contribute to the additional broadening of the OH tag lines. Partial turbulent transport may also attribute to the widened OH tag lines.

One can compute the turbulent diffusion coefficient, D_{T} from the turbulent Schmidt number, $Sc_{\mathrm{T}} \equiv \upsilon_{\mathrm{T}}/D_{\mathrm{T}} = 0.7$ [28], where υ_{T} is the turbulent viscosity. Knowing that $\upsilon_{\mathrm{T}} = \mu_{\mathrm{T}}/\varrho$, and that $\upsilon_{\mathrm{T}} = 0.7D_{\mathrm{T}} = Kud$, one can now estimate the value of D_{T} for the specific flow conditions of this experiment. Empirically, one finds the eddy viscosity constant, $K \approx 0.018$ [29]. The resulting value for D_{T} based on the relation $D_{\mathrm{T}} = (Kud)/0.7$ is $90\ \mathrm{cm}^2/\mathrm{s}$ for $u = 28$ m/s and $d = 12.5$ mm. The corresponding binary molecular diffusion coefficient, D_{OH}, for OH into N_2 at 300 K as already reported is $0.27\ \mathrm{cm}^2/\mathrm{s}$. The much larger value for D_{T} than D_{OH} would suggest that the spreading out of the molecular grid lines could be attributed to small-scale turbulence effects where turbulent diffusion is prevalent. Based on the values of $D_{\mathrm{T}} = 90\ \mathrm{cm}^2/\mathrm{s}$ and $w_0 \sim 0.5$ mm, the estimated tag width after $\tau = 30$ μs is $w \sim 1.32$ mm. However, such large line widenings are not observed, mostly due to the fact that our jet flow is not fully turbulent. This suggests that usage of a D_{T} estimate that is based on fully developed turbulent flow is not appropriate.

To determine a velocity-measurement uncertainty, it is assumed that the center of the diffusion-broadened displaced line can be estimated to within one-tenth of the tag line's width. Using the experimentally determined width of 0.6 mm, and assuming that the center of that broadened line can be measured to within 10% of its width, results in a displacement uncertainty of 0.06 mm, which is ∼ 12% of the displacement vector. Thus, for these conditions, the velocity can be estimated to within ∼ 12% of its theoretical value.

Increasing the delay time between the write and read lasers acts to weaken the tag line due to the chemical reactions that deplete the tag molecules' concentration. This decreases the signal-to-noise ratio (SNR) of the tag-line detection, where 'signal' is defined as the detected light per unit area of detection, and 'noise' is the typical shot-to-shot fluctuation in detected light per unit area, not due to the tag line. The SNRs as a function of delay time between the write and read lasers were studied and are shown in Fig. 5, which is for room-temperature (297 K) quiescent air. In this figure, a common background was always subtracted from all experimental signal measurement points. The average tag-line signal (not affected by diffusion) was then divided by the largest noise fluctuation to obtain the SNR values, which are plotted as a function of delay time. Previous works have quantified the SNR for crossing points in simulated flow tagging grids as a function of pixel intensity and grid-intersection angle [30],

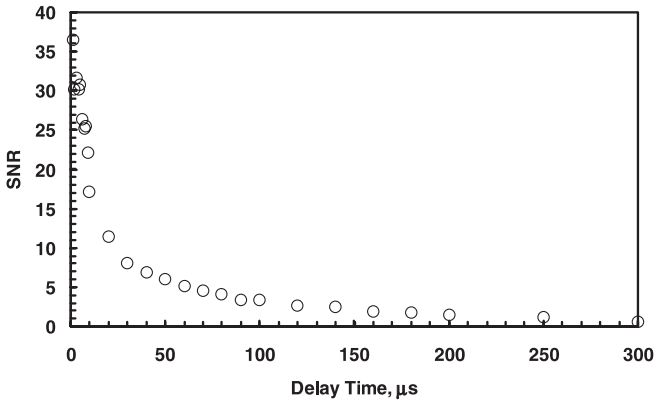

FIGURE 5 OH tag experimental signal to noise ratio (SNR) as a function of delay time (μs) between write and read laser. Signal is an average over a laser grid line segment and independent of diffusion. Experimental conditions: room temperature quiescent air (297 K, 40% RH)

and indicated that SNR values of 4 or higher were necessary to determine the location of the crossing point to sub-pixel accuracy of 0.1 or better for near-orthogonal intersection angles. The results in Fig. 5 show experimental HTV SNR levels for entire grid lines with near-orthogonal grid-intersection angles. As can be seen in Fig. 5, for very short delay times (0–20 μs) the SNR is very high (> 10) suggesting high confidence in locating accurately the displaced (and diffused) HTV grid lines. With increase in delay times (∼ 100 μs) the SNR drops to ∼ 4, and at delay times of 200 μs or greater, the SNR level is below 1. Although one can still observe the displaced HTV grid lines, accurate identification of crossing points (and, hence, unambiguous reference points in the flow) becomes difficult at these long delay times. These results suggest that low-temperature HTV is best suited for experimental flows where the interrogation times are of the order of tens of microseconds or less.

Based on the SNR given in Fig. 5, one can estimate the maximum number of lines that can be written in this flow. When tagging at shorter delay times (< 30 μs), one could expect to write about twice as many lines as the current case, $\sim 7 \times 7$ lines or ∼ 50 crossing points. More lines can be written in higher-temperature flows where the H_2O absorption is stronger. These laser lines could additionally be retroreflected to produce even more reference points in the measurement volume (as has been demonstrated with a single laser line [16]).

3 Summary and conclusions

In this work, a tunable 193-nm ArF excimer laser and a Nd–YAG-pumped tunable 308-nm frequency-doubled dye laser are used for molecular flow tagging in a low- (∼ 300 K) temperature air flow. The ArF excimer laser produces a grid of OH molecules that is displaced by the flowfield and imaged by the dye laser. The OH molecular grid is created via a single-photon process that yields very long lines (> 50 mm), compared to those generated from nonlinear processes. The dye laser accesses the strong $Q_1(1)$ line at 32 474.433 cm^{-1} (307.935 nm) in the $A^2\Sigma^+ (v' = 0) \leftarrow X^2\Pi_i (v'' = 0)$ OH band that compensates for the relatively weak 193-nm photodissociation cross sections of ground vibrational state H_2O. Multiline grids are used to demonstrate the feasibility of multipoint velocity measurements at room temperature. Lower-temperature HTV is applicable to situations where other similar methods may suffer from thermal decomposition, i.e. $T > 600$ K for O_3 (OTV) [14, 16]. These low-temperature HTV experiments use only one excimer laser (ArF), which does not need be tunable (i.e. in these experiments it was operated in its broadband mode) because the H_2O absorption band is a broad continuum with no distinct absorption lines. The Nd–YAG-pumped frequency-doubled dye laser is a relatively common laser system, thus rendering the new method economically and practically accessible to more researchers. Both the nontunable excimer laser and the Nd–YAG-pumped dye laser lower the initial investment cost of the system as compared to two tunable narrow-band excimer lasers. Proper selection of laser dyes with the same system allows probing of higher-temperature gas flows by pumping the $(1 \leftarrow 0)$, $(2 \leftarrow 0)$, $(3 \leftarrow 0)$, etc. transitions of the $(A^2\Sigma^+ \leftarrow X^2\Pi_i)$ OH band. Thus HTV could be viewed as the nonintrusive, instantaneous, molecular diagnostic method of choice in either low- (nonreacting) or high-temperature (reacting) flowfield environments at either atmospheric or higher pressures and with variable flow speeds.

ACKNOWLEDGEMENTS The authors gratefully acknowledge the support of NASA-Glenn (Grant No. NAG3-1984, Dr.R. Seasholtz, technical monitor), BMDO-ARO (DURIP Award No. DAAG55-98-1-0197, Dr.D. Mann, technical monitor), and AFOSR (DURIP Award No. F49620-99-1-0120, Dr.J. Tishkoff, technical monitor). The authors thank AEDC for use of the ArF excimer laser. We thank Mr.S. Nandula, Vanderbilt University, for his expert technical assistance.

Appendix: Air-chemistry reaction mechanisms

No.	Reaction[a]	A	n	E	Ref.
		H_2–O_2 chain reactions			
1	$H + O_2 = O + OH$	3.52×10^{16}	−0.70	1.71×10^4	[37]
2	$O + H_2 = H + OH$	5.08×10^4	2.67	6.29×10^3	[46]
3	$OH + H_2 = H_2O + H$	2.16×10^8	1.50	3.43×10^3	[44]
4	$O + H_2O = OH + OH$	5.08×10^{10}	0.946	1.703×10^4	[45]
		H_2–O_2 dissociation/recombination reactions			
5	$H_2 + M = H + H + M^b$	4.57×10^{19}	−1.40	1.04×10^5	[42]
6	$O + O + M = O_2 + M$	3.30×10^{14}	0.00	-9.60×10^2	[57]

7	$H+O+M=OH+M^b$	4.72×10^{18}	−1.00	0.0	[42]
8	$OH+H+M=H_2O+M^b$	2.21×10^{22}	−2.00	0.0	[42]
	Formation and consumption of HO_2				
9	$H+O_2(+M)=HO_2(+M)^{c,d}$				
	High-pressure limit, $k_\infty=$	4.52×10^{13}	0.00	0.0	[48]
	Low-pressure limit, $k_0=$	6.70×10^{19}	−1.42	0.0	[47]
	TROE values:	1.00	0.00	0.10×10^{91}	
10	$HO_2+O=O_2+OH$	1.75×10^{13}	0.00	-3.97×10^{2}	[42]
11	$HO_2+H=H_2+O_2$	6.62×10^{13}	0.00	2.13×10^{3}	[42]
12	$HO_2+H=OH+OH$	1.69×10^{14}	0.00	8.74×10^{2}	[42]
13	$HO_2+OH=H_2O+O_2$	1.90×10^{16}	−1.00	0.0	[33]
	Formation and consumption of H_2O_2				
14	$OH+OH(+M)=H_2O_2(+M)^c$				
	High-pressure limit, $k_\infty=$	7.53×10^{13}	−0.40	0.0	[49]
	Low-pressure limit, $k_0=$	2.213×10^{19}	−0.76	0.0	[49]
	TROE values:	0.672	0.00	0.10×10^{91}	[49]
15[e]	$HO_2+HO_2=H_2O_2+O_2$	4.20×10^{14}	0.00	1.20×10^{4}	[54]
	$HO_2+HO_2=H_2O_2+O_2$	1.30×10^{11}	0.00	-1.63×10^{3}	[54]
16	$H_2O_2+H=H_2O+OH$	1.00×10^{13}	0.00	3.59×10^{3}	[43]
17	$H_2O_2+H=HO_2+H_2$	4.82×10^{13}	0.00	7.95×10^{3}	[42]
18	$H_2O_2+O=OH+HO_2$	9.64×10^{6}	2.00	3.97×10^{3}	[42]
19[e]	$H_2O_2+OH=H_2O+HO_2$	1.00×10^{12}	0.00	0.0	[38]
	$H_2O_2+OH=H_2O+HO_2$	5.80×10^{14}	0.00	9.56×10^{3}	[38]
	O_3 reactions				
20	$O+O_2(+M)=O_3(+M)^{c,f}$				
	High-pressure limit, $k_\infty=$	1.69×10^{12}	0.00	0.0	[56]
	Low-pressure limit, $k_0=$	0.18×10^{22}	−2.80	0.0	[56]
	TROE values:	1.00	0.00	0.70×10^{3}	
21	$O+O_3=O_2+O_2$	4.81×10^{12}	0.00	4.09×10^{3}	[55]
22	$O_3+H=OH+O_2$	8.43×10^{13}	0.00	9.34×10^{2}	[55]
23	$O_3+OH=HO_2+O_2$	1.15×10^{12}	0.00	1.99×10^{3}	[55]
24	$O_3+HO_2=OH+2O_2$	8.43×10^{9}	0.00	1.19×10^{3}	[55]
	$O(^1D)^{g,h}$ reactions				
25	$O(^1D)+M_1=O+M_1{}^i$	1.20×10^{13}	0.00	-2.12×10^{2}	[32]
26	$O(^1D)+O_2=O+O_2S^g$	1.54×10^{13}	0.00	-1.33×10^{2}	[32]
27	$O(^1D)+O_2=O+O_2D^h$	6.02×10^{11}	0.00	0.0	[32]
28	$O(^1D)+O_3=2O_2$	1.46×10^{14}	0.00	0.0	[32]
29	$O(^1D)+O_3=2O+O_2$	7.23×10^{13}	0.00	0.0	[32]
30	$O+O_3=O_2+O_2S$	6.02×10^{12}	0.00	4.57×10^{3}	[32]
31	$O+O_3=O_2+O_2D$	1.69×10^{9}	0.00	4.57×10^{3}	[32]
	O_2S and O_2D reactions				
32	$O_2S+M_1=O_2+M_1{}^i$	1.30×10^{9}	0.00	0.0	[32]
33	$O_2S+O_2=O_2+O_2$	2.41×10^{7}	0.00	0.0	[32]
34	$O_2S+O_3=2O_2+O$	9.03×10^{12}	0.00	0.0	[32]
35	$O_2D+M_1=O_2+M_1{}^i$	2.40×10^{5}	0.00	0.0	[32]
36	$O_2D+O_2=O_2+O_2$	1.38×10^{4}	0.80	0.0	[32]
37	$O_2D+O_3=2O_2+O$	9.03×10^{12}	0.00	0.0	[32]
	NO_2 reactions				
38	$NO+O(+M)=NO_2(+M)^c$				
	High-pressure limit, $k_\infty=$	1.30×10^{15}	−0.75	0.0	[35]
	Low-pressure limit, $k_0=$	4.72×10^{24}	−2.87	1.55×10^{3}	[35]
	TROE values:	0.96	0.00	0.83×10^{4}	
39	$NO_2+O=O_2+NO$	3.91×10^{12}	0.00	-2.38×10^{2}	[35]
40	$NO_2+NO_2=2NO+O_2$	1.63×10^{12}	0.00	2.61×10^{4}	[35]
41	$HO_2+NO=NO_2+OH$	2.11×10^{12}	0.00	-4.79×10^{2}	[60]
42	$NO_2+H=NO+OH$	1.32×10^{14}	0.00	3.61×10^{2}	[41]
43	$O_3+NO=O_2+NO_2$	1.08×10^{12}	0.00	2.72×10^{3}	[55]
	NO_3 reactions				
44	$NO_2+O(+M)=NO_3(+M)^c$				
	High-pressure limit, $k_\infty=$	1.33×10^{13}	0.00	0.0	[35]
	Low-pressure limit, $k_0=$	1.49×10^{28}	−4.08	2.47×10^{3}	[35]
	TROE values:	0.83	0.00	0.32×10^{4}	
45	$NO_3+H=NO_2+OH$	6.00×10^{13}	0.00	0.0	[57]
46	$NO_3+O=NO_2+O_2$	1.00×10^{13}	0.00	0.0	[57]
47	$NO_3+OH=NO_2+HO_2$	1.43×10^{13}	0.00	0.0	[57]
48	$NO_3+HO_2=NO_2+O_2+OH$	1.50×10^{12}	0.00	0.0	[57]
49	$NO_3+NO_2=NO+NO_2+O_2$	5.00×10^{10}	0.00	2.44×10^{3}	[57]

50	$NO_3 + NO_3 = NO_2 + NO_2 + O_2$	5.12×10^{11}	0.00	4.84×10^3	[57]
51	$NO_3 + M = O_2 + NO + M^b$	2.05×10^8	1.00	1.21×10^4	[57]
52	$NO_2 + NO_2 = NO_3 + NO$	9.64×10^9	0.73	2.09×10^4	[35]
53	$O_3 + NO_2 = O_2 + NO_3$	7.22×10^{10}	0.00	4.87×10^3	[55]
	HNO reactions				
54	$NO + H(+M) = HNO(+M)^c$				
	High-pressure limit, $k_\infty =$	1.52×10^{15}	−0.41	0.0	[35]
	Low-pressure limit, $k_0 =$	8.96×10^{19}	−1.32	7.35×10^2	[35]
	TROE values:	0.82	0.0	0.10×10^{91}	
55	$NO + H_2 = HNO + H$	1.39×10^{13}	0.00	5.65×10^4	[35]
56	$HNO + O = OH + NO$	1.81×10^{13}	0.00	0.0	[35]
57	$HNO + OH = H_2O + NO$	4.82×10^{13}	0.00	9.94×10^2	[35]
58	$HNO + NO = N_2O + OH$	2.00×10^{12}	0.00	2.60×10^4	[36]
59	$HNO + NO_2 = HNO_2 + NO$	6.02×10^{11}	0.00	1.99×10^3	[35]
60	$HNO + HNO = H_2O + N_2O$	8.51×10^8	0.00	3.08×10^3	[40]
61	$HNO + O_2 = NO + HO_2$	1.00×10^{13}	0.00	2.50×10^4	[59]
	HNO_2 reactions				
62	$NO + OH(+M) = HNO_2(+M)^{c,j}$				
	High-pressure limit, $k_\infty =$	1.99×10^{12}	−0.05	-7.21×10^2	[35]
	Low-pressure limit, $k_0 =$	5.08×10^{23}	−2.51	-6.78×10^1	[35]
	TROE values:	0.62	0.00	0.10×10^{91}	
63	$HNO_2 + O = OH + NO_2$	1.20×10^{13}	0.00	5.96×10^3	[35]
64	$HNO_2 + H = H_2 + NO_2$	1.20×10^{13}	0.00	7.35×10^3	[35]
65	$HNO_2 + OH = H_2O + NO_2$	1.26×10^{10}	1.00	1.35×10^2	[35]
66	$HNO_2 + HNO_2 = NO + NO_2 + H_2O$	2.30×10^{12}	0.00	8.40×10^3	[58]
	HNO_3 reactions				
67	$NO_2 + OH(+M) = HNO_3(+M)^c$				
	High-pressure limit, $k_\infty =$	2.41×10^{13}	0.00	0.0	[35]
	Low-pressure limit, $k_0 =$	6.42×10^{32}	−5.49	2.35×10^3	[35]
	TROE values:	0.84	0.00	0.17×10^4	
68	$HO_2 + NO + M = HNO_3 + M$	2.23×10^{12}	−3.50	2.20×10^3	[61]
69	$HNO_3 + OH = H_2O + NO_3$	1.03×10^{10}	0.00	-1.24×10^3	[57]
70	$NO_3 + HO_2 = O_2 + HNO_3$	5.60×10^{11}	0.00	0.0	[57]
	N_2O reactions				
71	$N_2O(+M) = N_2 + O(+M)^{c,k}$				
	High-pressure limit, $k_\infty =$	7.91×10^{10}	0.00	5.60×10^4	[51]
	Low-pressure limit, $k_0 =$	8.80×10^{14}	0.00	5.77×10^4	[51]
72	$N_2O + O = O_2 + N_2$	1.00×10^{14}	0.00	2.80×10^4	[52]
73	$N_2O + O = 2NO$	1.00×10^{14}	0.00	2.80×10^4	[52]
74	$N_2O + NO = N_2 + NO_2$	1.00×10^{14}	0.00	4.97×10^4	[53]
75	$NO_2 + NO = N_2O + O_2$	1.00×10^{12}	0.00	6.00×10^4	[50]
	N and NO reactions				
76	$NO + M = N + O + M$	1.45×10^{15}	0.00	1.48×10^5	[35]
77	$NO + O = O_2 + N$	1.81×10^9	1.00	3.88×10^4	[35]
78	$NO + NO = N_2 + O_2$	1.30×10^{14}	0.00	7.56×10^4	[50]
79	$O + N_2 = NO + N$	1.81×10^{14}	0.00	7.61×10^4	[53]
80	$N + OH = NO + H$	3.80×10^{13}	0.00	0.0	[36]
81	$N + HO_2 = NO + OH$	1.00×10^{13}	0.00	2.00×10^3	[50]
82	$N + HNO = N_2O + H$	5.00×10^{10}	0.50	3.00×10^3	[50]
83	$N + N_2O = N_2 + NO$	1.00×10^{13}	0.00	1.99×10^4	[50]
84	$N + NO_2 = N_2 + O_2$	1.00×10^{12}	0.00	0.0	[50]
85	$N + NO_2 = NO + NO$	4.00×10^{12}	0.00	0.0	[50]
86	$N + NO_2 = N_2O + O$	5.00×10^{12}	0.00	0.0	[50]
87	$N_2 + M = N + N + M$	2.30×10^{29}	−3.50	2.25×10^5	[53]
	'Ionic' reactions				
88	$NO^+ + e = N + O$	2.30×10^{18}	−0.40	0.0	[34]
89	$O_2^+ + e = O + O$	1.67×10^{20}	−0.60	0.0	[34]
90	$N_2^+ + e = N + N$	1.50×10^{18}	−0.40	0.0	[34]
91	$O^+ + e + M = O + M^l$	1.12×10^{27}	−2.50	0.0	[34]
92	$N^+ + e + M = N + M^l$	1.12×10^{27}	−2.50	0.0	[34]
93	$NO^+ + e + M = NO + M$	3.37×10^{27}	−2.50	0.0	[34]
94	$O_2^+ + e + M = O_2 + M$	3.37×10^{27}	−2.50	0.0	[34]
95	$N_2^+ + e + M = N_2 + M$	3.37×10^{27}	−2.50	0.0	[34]
96	$N_2^+ + NO = NO^+ + N_2$	2.00×10^{14}	0.00	0.0	[34]
97	$N_2^+ + O_2 = O_2^+ + N_2$	5.10×10^7	1.40	0.0	[34]
98	$N_2^+ + O = O^+ + N_2$	2.10×10^{11}	0.40	0.0	[34]
99	$N_2^+ + N = N^+ + N_2$	6.00×10^{11}	0.00	0.0	[39]
100	$N^+ + NO = NO^+ + N$	5.00×10^{14}	0.00	0.0	[34]
101	$N^+ + O_2 = O_2^+ + N$	1.40×10^{12}	0.60	0.0	[34]

102	$N^+ + O = O^+ + N$	6.00×10^{11}	0.00	0.0	[34]
103	$O^+ + NO = NO^+ + O$	3.25×10^{6}	1.70	0.0	[34]
104	$O^+ + O_2 = O_2{}^+ + O$	8.30×10^{8}	1.20	0.0	[34]
105	$O_2{}^+ + NO = NO^+ + O_2$	2.70×10^{14}	0.00	0.0	[34]
106	$O^+ + N_2 = NO^+ + N$	5.33×10^{5}	2.00	0.0	[34]
107	$N^+ + O_2 = NO^+ + O$	1.40×10^{12}	0.60	0.0	[34]
108	$O_2{}^+ + N = NO^+ + O$	7.20×10^{13}	0.00	0.0	[34]
109	$N_2{}^+ + O = NO^+ + N$	1.00×10^{13}	0.00	0.0	[34]

[a] $k = AT^n \exp(-E/RT)$; reaction rates for A are in (cm^3 mol s K) units, T (K), E (cal/mol)
[b] Efficiency factor for the collision partner of this pressure-dependent reaction is $\varepsilon_{NO_2} = 0.0$. All other species have efficiencies equal to unity
[c] For reactions showing low-(k_0) and high-(k_∞) pressure limit data, the Troe [31] form of rate constants for intermediate pressures is used. Troe values given, in order, are α, T^{***}, and T^*
[d] Efficiency factors for the collision partners of this pressure-dependent reaction are $\varepsilon_{H_2} = 2.5$, $\varepsilon_{H_2O} = 12.0$, $\varepsilon_{CO} = 1.9$, and $\varepsilon_{CO_2} = 3.8$. All other species have efficiencies equal to unity
[e] Reactions 15 and 19 are expressed as the sum of the two rate expressions
[f] Efficiency factor(s), ε_m, for the collision partner(s), M, of this pressure-dependent reaction are $\varepsilon_{O_2S}{}^g = 0.0$, $\varepsilon_{O_2} = 1.1$, and $\varepsilon_{O_2D}{}^h = 0.0$. All other species have efficiencies equal to unity
[g] $O_2S = O_2(b^1\Sigma_g^+)$
[h] $O_2D = O_2(a^1\Delta_g)$
[i] Efficiency factor for the collision partner of this pressure-dependent reaction is $\varepsilon_{O_2} = 0.0$. All other species have efficiencies equal to unity. $M_1 = N_2$, Ar
[j] Efficiency factor for the collision partner of this pressure-dependent reaction is $\varepsilon_{H_2O} = 5.0$. All other species have efficiencies equal to unity
[k] Efficiency factor for the collision partner of this pressure-dependent reaction is $\varepsilon_{H_2O} = 12$. All other species have efficiencies equal to unity
[l] Efficiency factors for the collision partners of this pressure-dependent reaction are $\varepsilon_{N_2} = 3.0$, $\varepsilon_{O_2} = 3.0$, $\varepsilon_{NO} = 3.0$, and $\varepsilon_E = 2.0$. All other species have efficiencies equal to unity

REFERENCES

1 R.M. Measures: J. Appl. Phys. **39**, 5232 (1968)
2 M. Zimmermann, R.B. Miles: Appl. Phys. Lett. **37**, 885 (1980)
3 J.C. McDaniel, B. Hiller, R.K. Hanson: Opt. Lett. **8**, 51 (1983)
4 W. Marinelli, W.J. Kessler, M.G. Allen, S.J. Davis, S. Arepalli: 29th AIAA Aerosp. Sci. Meet. Exhib., Reno, NV, 1991, paper 91-0358
5 P.H. Paul, M.P. Lee, R.K. Hanson: Opt. Lett. **14**, 417 (1989)
6 R.G. Seasholtz, F.J. Zupanc, S.J. Schneider: J. Propul. Power **8**, 935 (1992)
7 J.N. Forkey, N.D. Finkelstein, W.R. Lempert, R.B. Miles: AIAA J. **34**, 442 (1996)
8 B. Hiller, R.A. Booman, C. Hassa, R.K. Hanson: Rev. Sci. Instrum. **55**, 1964 (1984)
9 B. Stier, M.M. Koochesfahani: Exp. Fluids **26**, 297 (1999)
10 C. Orlemann, C. Schulz, J. Wolfrum: Chem. Phys. Lett. **307**, 15 (1999)
11 S. Krüger, G. Grünefeld: Appl. Phys. B **69**, 509 (1999)
12 L.R. Boedecker: Opt. Lett. **14**, 473 (1989)
13 R.B. Miles, J. Grinstead, R.H. Kohl, G. Diskin: Meas. Sci. Technol. **11**, 1272 (2000)
14 L.A. Ribarov, J.A. Wehrmeyer, F. Batliwala, R.W. Pitz: AIAA J. **37**, 708 (1999)
15 J.A. Wehrmeyer, L.A. Ribarov, D.A. Oguss, R.W. Pitz: Appl. Opt. **38**, 6912 (1999)
16 R.W. Pitz, J.A. Wehrmeyer, L.A. Ribarov, D.A. Oguss, F. Batliwala, P.A. DeBarber, S. Deusch, P.E. Dimotakis: Meas. Sci. Technol. **11**, 1259 (2000)
17 K. Kohse-Höinghaus: Prog. Energy Combust. Sci. **20**, 203 (1994)
18 J.M. Seitzman, R.K. Hanson: AIAA J. **31**, 513 (1993)
19 A.M. Bass, H.P. Broida: Natl. Bur. Stand. Circ. **541**, 1 (1953)
20 G.H. Dieke, H.M. Crosswhite: J. Quantum Spectrosc. Radiat. Transfer **2**, 97 (1962)
21 LIFBASE (version 1.6), http: //www.sri.com/cem/lifbase
22 M.S. van Hemert, R. van Harrevelt: private communication, Leiden Institute of Chemistry, Gorlaeus Laboratories, Leiden, The Netherlands (1999)
23 A.E. Lutz, R.J. Kee, J.A. Miller: Sandia Rep. SAND87-8248×UC-4 (1988)
24 H. Tennekes, J.L. Lumley: *A First Course in Turbulence* (MIT Press, Cambridge, MA 1972)
25 V.L. Streeter, E.B. Wylie: *Fluid Mechanics* (McGraw-Hill, New York 1985)
26 S.H. Stårner, R.W. Bilger: Combust. Sci. Technol. **21**, 259 (1980)
27 R.B. Miles, W. Lempert, B. Zhang: Fluid Dyn. Res. **8**, 9 (1991)
28 R.W. Bilger: AIAA J. **20**, 962 (1982)
29 F. White: *Viscous Fluid Flow* (McGraw-Hill, New York 1991)
30 C.P. Gendrich, M.M. Koochesfahani: Exp. Fluids **22**, 67 (1996)
31 R.G. Gilbert, K. Luther, J. Troe: Ber. Bunsenges. Phys. Chem. **87**, 169 (1983)
32 B. Freisinger, U. Kogelschatz, J.H. Schäfer, J. Uhlenbusch, W. Viöl: Appl. Phys. B **49**, 121 (1989)
33 T.J. Kim, R.A. Yetter, F.L. Dryer: Proc. Combust. Inst. **25**, 759 (1994)
34 *Reaction Rate Handbook*, 2nd edn. (DNA 1948H) (Defense Nuclear Agency, Washington, D.C., USA 1979)
35 W. Tsang, J.T. Herron: J. Phys. Chem. Ref. Data **20**, 609 (1991)
36 J.A. Miller, C.T. Bowman: Prog. Energy Combust. Sci. **15**, 287 (1989)
37 D.A. Masten, R.K. Hanson, C.T. Bowman: J. Phys. Chem. **94**, 7119 (1990)
38 H. Hippler, J. Troe: Chem. Phys. Lett. **192**, 333 (1992)
39 R.C. Brown, K.D. Annen, C.E. Kolb: ARI-RR-771 (Aerodyne Research, Billerica, MA 1989)
40 Y. He, M.C. Lin: Int. J. Chem. Kinet. **24**, 743 (1992)
41 T. Ko, A. Fontijn: J. Phys. Chem. **95**, 3984 (1991)
42 W. Tsang, R.F. Hampson: J. Phys. Chem. Ref. Data **15**, 1087 (1986)
43 J. Warnatz: in *Combustion Chemistry* (Springer, New York 1984)
44 J.V. Michael, J.W. Sutherland: J. Phys. Chem. **92**, 3853 (1988)
45 A. Lifschitz, J.V. Michael: Proc. Combust. Inst. **23**, 59 (1990)
46 J.W. Sutherland, J.V. Michael, A.N. Pirraglia, F.L. Nesbitt, R.B. Klemm: Proc. Combust. Inst. **21**, 929 (1986)
47 M.W. Slack: Combust. Flame **28**, 241 (1977)
48 C.J. Cobos, H. Hippler, J. Troe: J. Phys. Chem. **89**, 342 (1985)
49 L. Brouwer, C.J. Cobos, J. Troe, H.R. Dubal, F.F. Crim: J. Chem. Phys. **86**, 6171 (1987)
50 C.F. Melius: in *Chemistry and Physics of Energetic Materials* (Kluwer Academic, Dordrecht 1990)
51 M.T. Allen, R.A. Yetter, F.L. Dryer: Int. J. Chem. Kinet. **27**, 883 (1995)
52 D.L. Baulch, D.D. Drysdale, D.G. Horne, A.C. Lloyd: *Evaluated Kinetic Data for High Temperature Reactions* (Butterworths, London 1973)
53 R.K. Hanson, S. Salimian: in *Combustion Chemistry* (Springer, New York 1984)
54 H. Hippler, J. Troe, J. Willner: J. Chem. Phys. **93**, 1755 (1990)
55 R. Atkinson, D.L. Baulch, R.A. Cox, R.F. Hampson, Jr., J.A. Kerr, J. Troe: J. Phys. Chem. Ref. Data **21**, 1125 (1992)
56 R. Atkinson, D.L. Baulch, R.A. Cox, R.F. Hampson, Jr., J.A. Kerr, J. Troe: J. Phys. Chem. Ref. Data **18**, 881 (1989)
57 W.G. Mallard, F. Westley, J.J. Herron, R.F. Hampson: NIST Chemical Kinetics Database, version 6 (NIST Standard Reference Data, Gaithersburg, MD 1994)
58 M.C. Lin, Y. He, C.F. Melius: Int. J. Chem. Kinet. **24**, 489 (1987)
59 J.A. Miller, C.T. Bowman: Int. J. Chem. Kinet. **23**, 289 (1991)
60 C.J. Howard: J. Am. Chem. Soc. **102**, 6937 (1980)
61 M.G. Michaud, P.R. Westmoreland, A.S. Feitelberg: Proc. Combust. Inst. **24**, 879 (1992)